ACS APPLIED MATERIALS & INTERFACES

RESEARCH ARTICLE

www.acsami.org

Migration Kinetics of Oxygen Vacancies in Mn-Modified $BiFeO_3$ Thin Films

Jiagang Wu,*[,†,‡] John Wang,[‡] Dingquan Xiao,[†] and Jianguo Zhu[†]

[†]Department of Materials Science and Engineering, Sichuan University, 610064, P. R. China

[‡]Department of Materials Science and Engineering, National University of Singapore, 117574, Singapore

ABSTRACT: Migration kinetics of oxygen vacancies in $BiFe_{0.95}Mn_{0.05}O_3$ thin film were investigated by the temperature -dependent leakage current as well as the electric field and temperature-dependent impedance spectroscopy. The $BiFe_{0.95}Mn_{0.05}O_3$ is of an abnormal leakage behavior, and an Ohmic conduction is observed regardless of varied temperatures and electric fields. The temperature-dependent impedance spectroscopy under different resistance states is used to illuminate different leakage behavior between $BiFe_{0.95}Mn_{0.05}O_3$ and pure $BiFeO_3$. The impedance spectroscopy under a high resistance state shows that the first ionization of oxygen vacancies is responsible for the dielectric relaxation and electrical conduction of $BiFe_{0.95}Mn_{0.05}O_3$ in the whole temperature range of 294 to 474 K; the $BiFeO_3$ exhibits similar dielectric relaxation and electrical conduction behavior in the low-temperature range of 294−374 K, whereas the short-range motion of oxygen vacancies was involved in the high-temperature range of 374−474 K. The impedance spectroscopy under a low resistance state demonstrates that the dielectric relaxation and conduction mechanisms almost keep unchanged for $BiFe_{0.95}Mn_{0.05}O_3$, whereas the hopping electrons of $Fe^{2+}-V_O^{\bullet}-Fe^{3+}$ and $Fe^{2+}-Fe^{3+}$ are responsible for its dielectric relaxation and conduction mechanism of $BiFeO_3$. Different impedance spectroscopy under low and high resistance states confirms that an abnormal leakage behavior of $BiFe_{0.95}Mn_{0.05}O_3$ is related to different migration kinetics of oxygen vacancies, obviously differing from that of $BiFeO_3$.

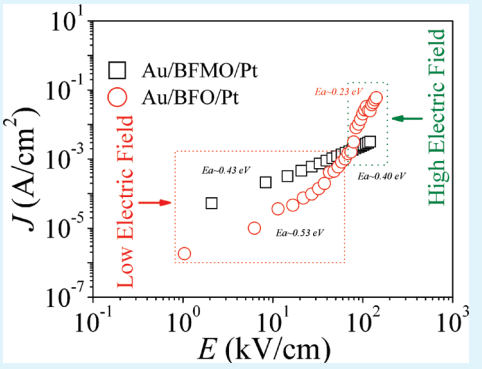

KEYWORDS: multiferroics, bismuth ferrite, mn, oxygen vacancy, impedance spectroscopy, ferroelectric properties

1. INTRODUCTION

Lead-free multiferroic $BiFeO_3$ (BFO) thin film exhibits a promising application in the ferroelectric random access memory, due to its giant remanent polarization of $P_r \approx 100\ \mu C/cm^2$,[1−3] a high Curie temperature of $T_c \approx 1104$ K,[4] and environmental friendliness.[5−8] In contrast, a fatal problem that seriously hinders the practical application of BFO is the high leakage current at room temperature.[9] Some attempts or new methods have been conducted to reduce the leakage current of BFO thin films.[1,2,10−15] Among those methods reported before, the site engineering (ions substitution) is a very promising tool to not only reduce leakage current but also improve the ferroelectric properties of BFO thin films.[9,12−14] The Mn^{3+} substitution for the Fe site is a leading candidate for improving the ferroelectric properties of BFO thin films by greatly reducing its room-temperature leakage current in a high electric field region,[16−18] and even a 256 Mbit has been fabricated by using a Mn-doped BFO thin film capacitor.[19] Although it is believed that the low leakage current in a high electric field region is responsible for the improvement in the polarization of BFO thin films,[17] the related physical mechanism underlying it is still an open question.

It is believed that the electrical behaviors of BFO-based thin films are correlated to the oxygen vacancies,[20−24] and especially the leakage current density in a high electric field region directly determines its ferroelectric behavior.[22] Recent research has also confirmed oxygen vacancies are responsible for the high leakage current of BFO thin films,[20−24] and the high leakage current for BFO results from the generation of a number of oxygen vacancies induced by the loss of bismuth and the shift of Fe^{3+} to Fe^{2+}. Oxygen vacancies, which easily migrate toward the electrode interface under the ac electric field, degrade the polarization of ferroelectric thin films by pinning the domain walls.[25−30] Because oxygen vacancies dominate the electrical behavior of BFO-based thin films, it would be therefore of a great value to study the migration kinetics of oxygen vacancies in BFO thin films by the complex impedance spectroscopy,[1,20] providing deep insights into how the oxygen vacancies modulate the electrical behavior of BFO thin films. In addition, the impedance spectroscopy under different resistance states in the present work is an effective tool for understanding the migration kinetics of oxygen vacancies in the Mn-modified BFO thin film ($BiFe_{0.95}Mn_{0.05}O_3$; BFMO) and illuminating the reason why the leakage behavior of BFMO is different from that of pure BFO,[17,31] where the dielectric relaxation and conduction mechanisms for BFMO were of little concern until now. As a result, these related works mentioned above undoubtedly help guide future research or the enhancement in the electrical properties and the understanding in the related

Received: March 25, 2011
Accepted: June 1, 2011
Published: June 15, 2011

dx.doi.org/10.1021/am2003747 | *ACS Appl. Mater. Interfaces* 2011, 3, 2504–2511

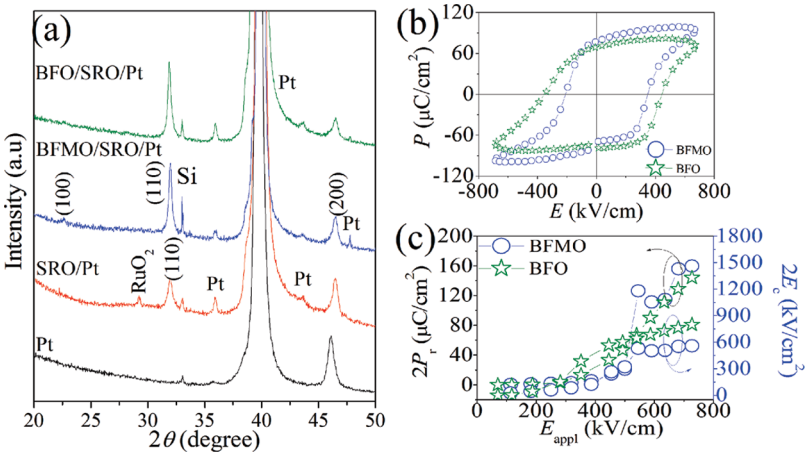

Figure 1. (a) XRD patterns for the BFMO, BFO, SRO, and Pt coated silicon substrate. (b) $P-E$ loop, and (c) $2P_r$ and $2E_c$ values vs applied electric fields of BFMO and BFO.

physical mechanisms of Mn-doped BFO thin films, which make it better apply in the high density data storage.

In this work, the BFMO thin film was deposited in situ on the $SrRuO_3$(SRO)/Pt(111)/TiO_2/SiO_2/Si(100) substrate by radio frequency (rf) sputtering. We focus on studying the physical mechanisms underlying the abnormal leakage behavior of the BFMO thin film by the migration kinetics of oxygen vacancies using the temperature-dependent impedance spectroscopy under low/high resistance states, and explain why the BFMO thin film has different leakage behavior as compared with that of pure BFO.

2. EXPERIMENTAL SECTION

The BFMO thin film was in situ deposited onto the SRO/Pt(111)/Ti/SiO_2/Si(100) substrate by using rf sputtering technique. A SRO buffer layer of ~100 nm in thickness was first grown in situ by rf sputtering on the Pt/TiO_2/SiO_2/Si(100) substrate at the substrate temperature of 680 °C, and then the BFMO thin film was deposited in situ on the SRO/Pt/TiO_2/SiO_2/Si(100) substrate at the substrate temperature of 570 °C. They were both deposited under a rf power of 120 W, and at a base pressure of 3.0×10^{-6} Torr and a deposition pressure of 10 mTorr with Ar and O_2 at a ratio of 4:1, giving rise to a growth rate of ~2.0 nm/min for the BFMO layer. The resultant thickness of BFMO was measured to be ~240 nm. For comparison, the pure BFO thin film was grown at the same deposition condition and substrate. Circular Au electrodes of 0.20 mm in diameter were sputtered on the film surface by using a shadow mask in order to investigate their electrical behavior.

The phase structure of thin films was analyzed by using X-ray diffraction (XRD) (Bruker D8 Advanced XRD, Bruker AXS Inc., Madison, WI, CuKa). The temperature -dependent leakage current of thin films was measured by using a Keithley meter (Keithley 6430, Cleveland, OH). The ferroelectric behavior of thin films was studied by using the Radiant precise workstation (Radiant Technologies, Medina, NY). An impedance analyzer (Solartron Gain phase Analyzer) was used to characterize the dielectric relaxation and conduction behavior of thin films.

3. RESULTS AND DISCUSSION

Figure 1a shows the XRD patterns of BFMO and BFO thin films as well as the SRO buffer layer, together with the Pt-coated silicon substrate. BFMO and BFO thin films are of a polycrystalline structure with a (110) orientation, and no secondary phases were detected. The BFO thin films, which are directly deposited on the Pt/TiO_2/SiO_2/Si(100) substrate without the SRO buffer layer, exhibit a polycrystalline structure with the formation of one or more secondary phases.[11] However, the (110) orientation together with a high phase purity in the present work was induced for BFMO and BFO by using the SRO buffer layer of (110) orientation, as shown in Figure.1a. Figure 1b shows the $P-E$ loop of Au/BFMO/SRO and Au/BFO/SRO capacitors, measured at room temperature and the frequency of 3.3 kHz. The square shaped $P-E$ hysteresis loop with a remanent polarization ($2P_r$) of ~159.8 μC/cm^2 and the coercive field ($2E_c$) of ~559.1 kV/cm were obtained for a BFMO thin film under an applied electric field of ~727.0 kV/cm, whereas the pure BFO thin film with a slight roundish shape exhibit a lower $2P_r$ value and a higher $2E_c$ value. The enhancement in $2P_r$ value of BFMO could be attributed to the improvement of the breakdown characteristic and the low leakage current density in the high electric field region,[17] together with a (110) orientation.[13] Figure 1(c) shows the maximum electric field dependence of $2P_r$ and $2E_c$ values for BFMO and BFO. The $2P_r$ value of BFMO seems to reach saturation for the maximum applied electric field higher than ~500 kV/cm, and reaches a maximum value of $2P_r$~159.8 μC/cm^2 at the applied electric field of ~727.0 kV/cm. However, the BFO thin film is difficult to reach saturation due to a high leakage current density. This $2P_r$ value of BFMO is much better than that of the pure BFO thin film, and is also compared with those of (110)-oriented BFO thin films deposited on SRO/$SrTiO_3$(110) substrates.[2,13] It is of great interest to note that the asymmetrical $P-E$ curve is demonstrated for the BFMO thin film. Two factors should contribute to the asymmetrical $P-E$ curve of the BFMO thin film. First, the $P-E$ hysteresis curve of the BFMO ferroelectric capacitor with asymmetric electrode materials is shifted due to the different work function between the top (Au) and bottom (SRO) electrodes.[32,33] Second, an internal field within the BFMO ferroelectric thin film is built by the imprint process. Electrical charges trapped at the electrode and ferroelectric interfaces during the imprint stress are responsible for the internal field build-up and screen the spontaneous polarization internally.[34]

Panels a and b in Figure 2 show the $\log(I)-\log(V)$ curves of the BFMO thin film, measured at negative and positive bias in the temperature range of 294−374 K. At room temperature, the BFMO thin film is subject to an Ohmic conduction with the

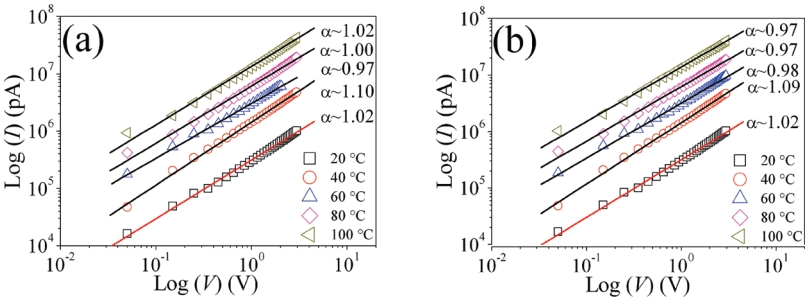

Figure 2. Log I vs log V curves of BFMO as a function of measurement temperature in (a) negative and (b) positive directions.

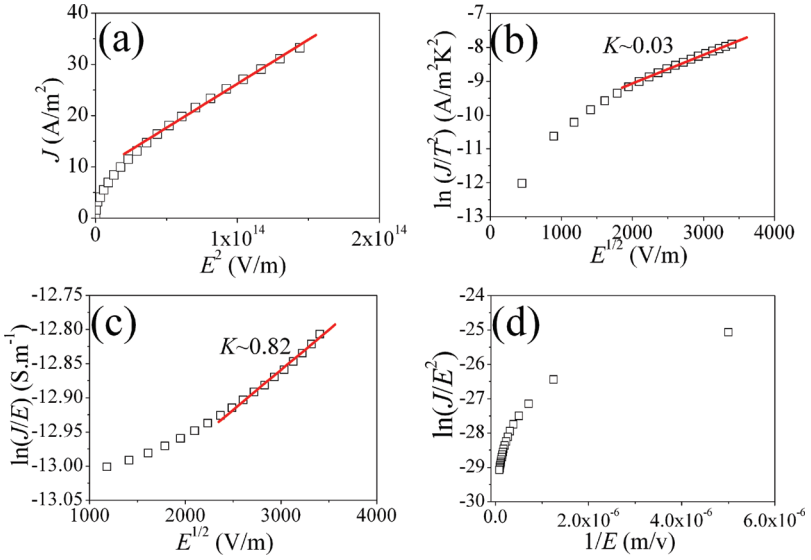

Figure 3. Various fits of these data are shown to determine the leakage mechanism at positive position: (a) SCLC, (b) Schottky barrier, (c) Poole−Frenkel emission, and (d) F−N tunneling.

exponentials of a∼1 regardless of positive and negative bias, as shown in the precision for the Ohmic fitting in panels a and b in Figure 2. In addition, the a value remained constant with rising temperature from 294 to 374 K, confirming the temperature-independent leakage mechanisms for BFMO. Therefore, the Ohmic conduction is responsible for BFMO regardless of negative and positive bias.

In the past, some possible mechanisms were used to characterize the leakage behavior of BFO thin films, where two kinds of bulk-limited and interface-limited conductions are included. Of all the possible mechanisms, four mechanisms are commonly observed in other perovskite oxides, such as the space-charge-limited conduction (SCLC), interface-limited Schottky emission, bulk-limited Poole-Frenkel (PF) emission, and the interface-limited Fowler−Nordheim (F−N) tunneling. They could be described by the following eqs 1−4.[35−38]

$$J_{\mathrm{SCLC}} = \frac{9\mu\varepsilon_r\varepsilon_0}{8d}E^2 \quad (1)$$

$$J_S = AT^2e - \frac{\varphi - \sqrt{q^3E/4\pi\varepsilon_0K}}{K_BT} \quad (2)$$

$$J_{\mathrm{PF}} = BEe - \frac{E_I - \sqrt{q^3E/\pi\varepsilon_0K}}{K_BT} \quad (3)$$

$$J_{\mathrm{FN}} = CE^2e^{\frac{-D^2\sqrt{\varphi_i{}^3}}{E}} \quad (4)$$

where K is the optical dielectric permittivity, and A, B, and C are the constants; φ, E_I, and φ_i are the height of Schottky barrier, the trap ionization energy, and potential barrier height, respectively. In the present work, we want to know whether other leakage mechanisms are involved into the BFMO thin film except for the Ohm conduction. According to eq 1, it was plotted as J vs E_2 for identifying the SCLC mechanism of the BFMO thin film at a positive electric field. As shown in Figure 3a, a linear region was clearly observed, confirming the involvement of the Ohmic conduction into the BFMO thin film. Similar analysis on the leakage behavior of the BFMO thin film was carried out by using eqs 2−4 for determining whether the Schottky barrier, PF emission, or F−N tunneling dominates the leakage current of the BFMO thin film. The optical dielectric permittivity (K) value can be considered in order to further analyze the operating leakage mechanism underlying the BFMO thin film, where the K can be derived from the slope of these plots in a linear fitting region. The refraction index (n) is usually determined to be ∼2.5 for BFO,[39] and a K value is calculated to be ∼6.25 by the equation of $K = n^2$.[39] The K values of ∼0.03 and 0.82 obtained from the Schottky and PF plots b and c in Figure 3 are greatly deviated from that reported for BFO, indicating that the Schottky and PF

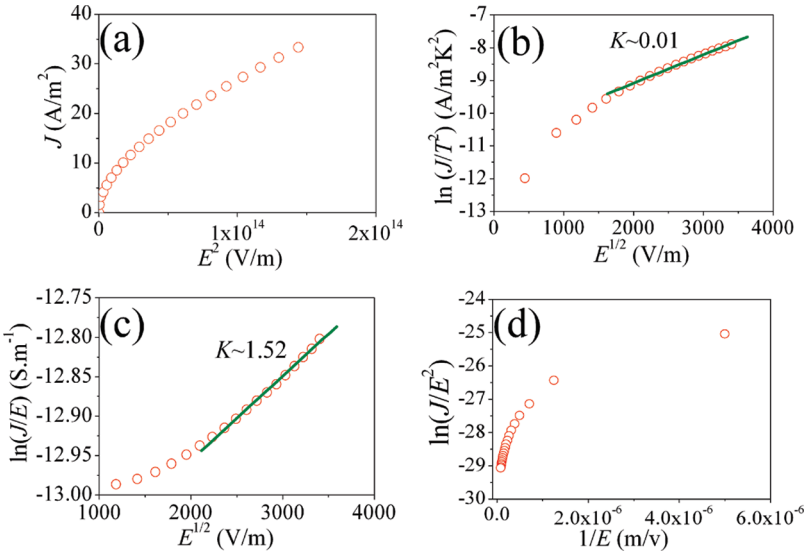

Figure 4. Various fits of these data are shown to determine the leakage mechanism at negative position: (a) SCLC, (b) Schottky barrier, (c) Poole−Frenkel emission, and (d) F−N tunneling.

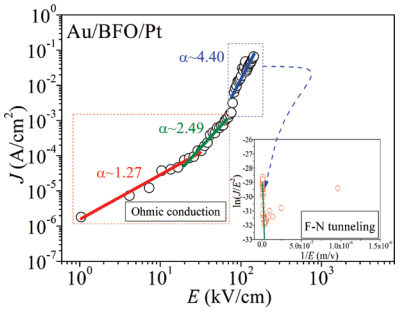

Figure 5. Log J vs log E curves of BFO thin films, where the insert is F−N tunneling.

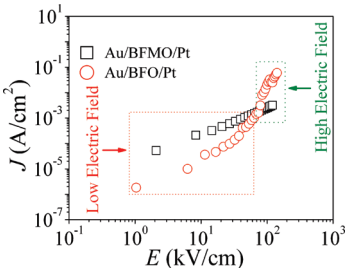

Figure 6. Leakage current density vs electric field characteristics of BFO and BFMO.

emission can be ruled out for BFMO of this work. Subsequently, we identify if the interface-limited F−N tunneling is involved into the leakage behavior of BFMO. Figure 3d shows the ln (J/E^2) as a function of $1/E$ of the BFMO thin film, according to eq 4. As shown in Figure 3d, the interface-limited F−N tunneling cannot dominate the leakage behavior of BFMO. The same analysis was also conducted for the BFMO thin film at a negative electric field, as plotted in Figures 4a−d. The interface-limited Schottky emission, bulk limited PF emission, or the interface-limited F−N tunneling cannot also dominate the leakage behavior of the BFMO thin film at a negative electric field. Therefore, the only Ohmic conduction governs the leakage behavior of the BFMO thin film at varying temperatures and electric fields, and the Ohmic conduction also largely contributes to the enhancement of ferroelectric behavior of the BFMO thin film. It has been reported that the Pt/BFO/SRO capacitor is of the Poole−Frenkle emission and Fowler−Nordheim tunneling,[40] and the Poole-Frenkel emission is involved into Pt/SRO/BFO/SRO/DSO structures,[41] which are different from the BFMO thin film in our work. Figure 5 plots the log(J)−log(E) curves of the Au/BFO/SRO thin film, measured at a positive electric field and room temperature. The BFO thin film is subject to a SCLC behavior in a low electric field region, while the interface-limited F−N tunneling dominates its leakage behavior in a high electric field region, as shown in the insert of Figure 5. Therefore, the introduction of Mn changes the leakage behavior of BFO thin films in this work.

The J−E curves of BFMO are obviously different from that of BFO in a low/high electric field region. Figure 6 plots the leakage current density vs electric field curves of Au/BFO/SRO and Au/BFMO/SRO capacitors, measured at room temperature. In the low electric field region, the BFO thin film has a lower leakage current density than that of BFMO. In contrast, the much lower leakage current density is observed for BFMO as compared with that of BFO in a high electric field region, indicating that the breakdown characteristic is improved by the Mn substitution for the Fe site in BFO. Similar phenomenon has been observed elsewhere.[17] Subsequently, we focus on the investigation of the physical mechanism underlying the abnormal leakage behavior in BFMO by the temperature-dependent impedance spectroscopy under different resistance states.

Although the leakage behavior of BFMO is identified to be an Ohmic conduction, the migration kinetics of charge carriers underlying the abnormal leakage behavior is not well-established. In the present work, the dielectric relaxation and

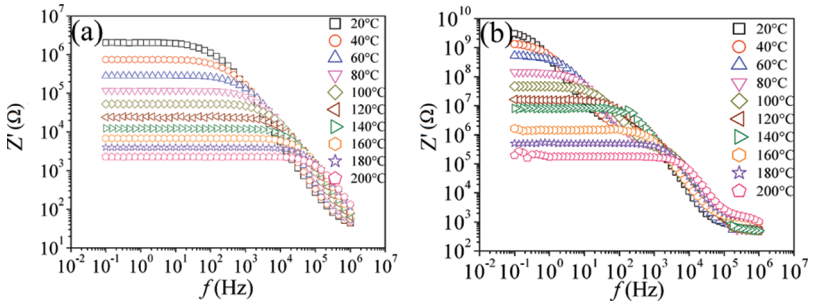

Figure 7. Variation in the real part of the impedance of (a) BFMO and (b) BFO thin films.

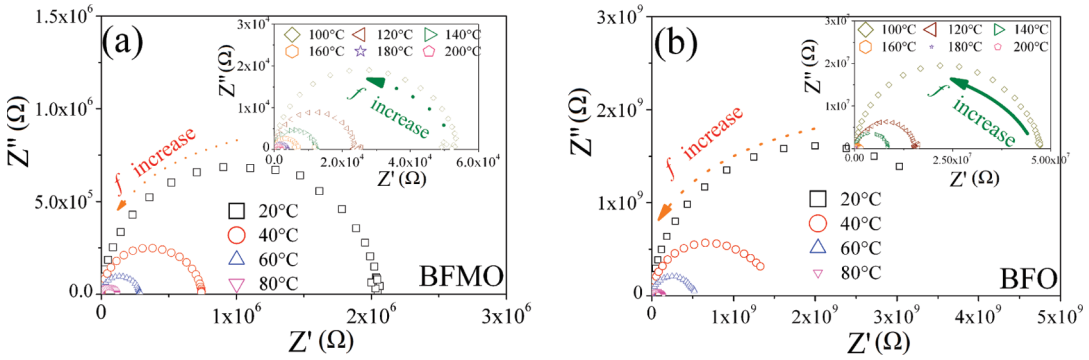

Figure 8. Cole−Cole plot of Z' versus Z'' over a wide frequency range (1×10^{-1} Hz to 1×10^{6} Hz) of BFMO and BFO thin films at different temperatures (294−474 K).

conduction behavior of charge defects in BFO and BFMO were investigated by the complex impedance spectroscopy under different resistance states. Our objective is to improve the electrical properties by controlling the density and the migration of charge carriers (oxygen vacancies). First, we carried out the impedance analysis under a high resistance state. Panels a and b in Figure 7 plot the frequency dependence of the real part of impedance (Z') of BFMO and BFO at various temperatures of 294−474 K, respectively. Their magnitudes of Z' decrease with an increase in both frequencies as well as temperatures, indicating an increase in ac conductivity with increasing temperatures and frequencies. The frequency dependence of the conductivity can be described by the power-law relationship.[42]

$$\sigma(\omega) = \sigma(0) + A\omega^{s} \qquad (5)$$

where $\sigma(\omega)$ and $\sigma(0)$ represent the total conductivity and the frequency-independent dc conductivity, respectively; the ω is angular frequency; the A and s are angular frequency and the temperature and material dependent parameters ($0< s < 1$), respectively. With rising temperature, the flattened regions become wider and are shifted toward a higher frequency, and the frequency-independent plateau-like region is assigned to the frequency-independent conductivity [$\sigma(0)$], indicating the involvement of frequency-independent σ_{ac}. A frequency-dependent conductivity region [$\sigma(\omega) \sim A\omega^{s}$] is also clearly observed with increasing frequencies. In addition, the flattened regions in the low-frequency region for BFMO become much wider as compared to that of BFO with rising temperature. The BFMO has a higher conductivity (lower Z'). Bowen[43] has shown that the ac current flows through conductive paths (resistors) and is frequency-independent at low frequencies ($R-C$). At higher frequencies ($R \sim wC$), the current begins to flow through capacitive regions, and the conductivity becomes frequency dependent. Since BFMO is more conductive, then the frequency independent region is present at higher frequencies. However, the BFMO thin film exhibits a lower resistivity than that of the BFO film at the same measurement temperature. This result is in agreement with their leakage current in a low electric field region, further confirming that the BFMO thin film has a higher leakage current as compared with that of the BFO thin film at a low electric field region, as shown in Figure 6.

Figure 8 shows the Cole−Cole plot of Z' versus Z'' over a wide frequency range (1×10^{-1} to 1×10^{6} Hz) at varying temperatures (294−474 K). Only a resolved semicircular arc can be observed, which is assigned to the response of grain,[44] and the impedance decreases with rising temperature from 294 to 474 K, as shown in panels a and b in Figure 8. For BFMO, the slope of the lines decreases with rising temperature, and reaches real (Z') axis at the temperature of 294 K, indicating the formation of a semicircle. However, a semicircle for BFO was formed only at a higher temperature of above 314 K. The peak height of Z' vs Z'' plots is determined by R_b, so the gradual decrease in the magnitude of Z'' indicates a decrease in the resistance with rising temperature, as confirmed by the shrinking semicircles in Cole−Cole plots. That is, the semicircle becomes much smaller with rising temperature, indicating the increase in the conductivity of the samples.

Figure 9a plots the inverse of the peak frequencies (relaxations time τ: $\tau = 1/2\pi f_{max}$) as a function of temperature for BFO and BFMO. The dielectric relaxation activation energy (E_R) value

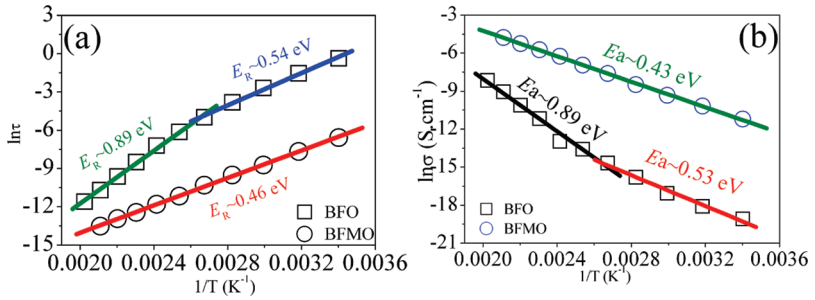

Figure 9. Arrhenius plots of (a) ln τ vs $1/T$ and (b) ln σ vs $1/T$ plots for the BFMO and BFO thin films under a high resistance state.

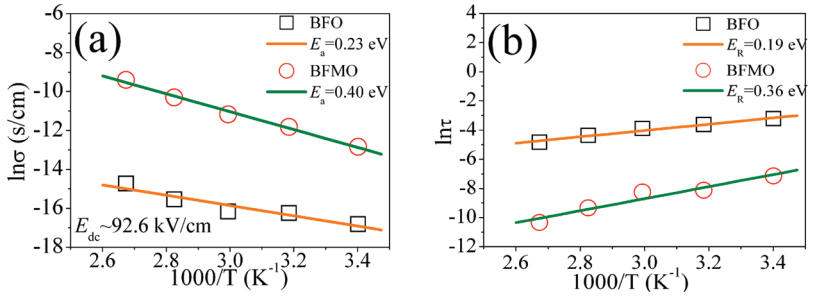

Figure 10. Arrhenius plots of (a) ln σ vs $1/T$ and (b) ln τ vs $1/T$ plots for the BFMO and BFO thin films under a low resistance state.

can be calculated according to the Arrhenius equation.[45]

$$\tau = \tau_o \exp(E_R/k_B T) \quad (6)$$

where τ_o is the relaxation time at infinite temperature, k_B is the Boltzmann constant, and T is the absolute temperature. An E_R value of ~0.46 eV is obtained for BFMO at the temperature of 294−474 K, whereas the BFO exhibits an E_R value of ~0.54 eV at the temperature of 294−374 K and an E_R value of ~0.89 eV at the temperature of 374−474 K. Different E_R values represent different dielectric relaxation mechanisms for BFO and BFMO. The E_R value in BFMO suggests the involvement of the first ionization of oxygen vacancies, the first ionization of oxygen vacancies is also involved into BFO at the temperature of 294−374 K, and the short-range oxygen vacancies at the temperature of 374−474 K. Therefore, the Mn substitution changes the type of the dielectric relaxation of BFO. Figure 9b plots the Arrhenius plot of ln σ vs $1/T$ of BFO and BFMO thin films. The temperature -dependent *dc* conductivity can be described by the Arrhenius equation.

$$\sigma_{dc} = \sigma_{dco} \exp(-E_a/k_B T) \quad (7)$$

where σ_o is a constant and E_a is the electrical conduction activation energy. The E_a value of BFMO was 0.43 eV at the temperature of 294−474 K, indicating that the first ionization of oxygen vacancies is still responsible for the electrical conduction regardless of varying temperatures. However, the E_a value of BFO depends on the measurement temperature, that is, the E_a value is ~0.53 eV for the temperature range of 294−374 K, and the value is ~0.89 eV for the temperature range of 374−474 K. The first ionization of oxygen vacancies is responsible for the electrical conduction of BFMO, whereas the first ionization of oxygen vacancies and the short-range oxygen vacancies was involved into the electrical conduction of BFO at the temperature of 294−374 and 374−474 K, respectively. In the present work, the E_a value well-matches the E_R value, respectively, for the BFO or BFMO thin film, confirming that the same type of charge carriers is responsible for both dielectric relaxation and electrical conduction. The activation energy is correlated to the density of oxygen vacancies,[46] that is, *E*is ~2.0 eV for stoichiometric ABO_3, ~1.0 eV for $ABO_{2.95}$, ~0.5 eV for $ABO_{2.9}$, and ~0 for $ABO_{2.8}$. Under a high resistance state, the BFMO thin film has a lower activation energy, indicating the involvement of a higher density of oxygen vacancies in BFMO. This result is also well in agreement with the fact that the BFMO thin film has a higher leakage current at room temperature in a low electric field region as compared with that of BFO.

It is very important to investigate the migration kinetics of oxygen vacancies under an external driving electric fields for better understanding the leakage behavior of the BFMO thin film. In the present work, the impedance spectroscopy under a *dc* electric field of ~92.6 kV/cm is used to identify the difference in the response of electrical conduction behavior of BFO and BFMO, and further understand the migration kinetics of oxygen vacancies in low and high resistance states. Panels a and b in Figure 10 show the Arrhenius plots of ln σ and ln τ vs $1000/T$ plots for the BFO and BFMO thin films under the *dc* electric field of ~92.6 kV/cm. The variation of the conductivity as a function of temperature is plotted in Figure 10a. Their conductivity increases with rising temperature. The E_a values of BFO and BFMO are 0.23 and 0.40 eV, respectively, indicating that the hopping electrons and the first ionization of oxygen vacancies are respectively involved into the conduction behavior of BFO and BFMO under a low resistance state. Comparing Figure 9b with Figure 10a, under an external *dc* electric field, the E_a value decreases dramatically from ~0.53 to 0.23 eV for BFO, whereas the E_a value almost keeps unchanged for BFMO. The E_a values under different resistance states indicate the involvement of the different conduction mechanisms into two films, and the higher E_a value indicates that the conducting electrons are difficultly

activated. In the present work, the E_a value of BFMO is higher than that of BFO at a low resistance state, indicating it is more difficult to activate the conducting electrons for BFMO under the same electric field. Figure 10b shows the Arrhenius plot of $\ln\tau$ vs $1000/T$ plots for the BFMO and BFO thin films under the *dc* electric field of ~92.6 kV/cm. Similarity to the change of the E_a values at different resistance states, the E_R value also almost keeps unchanged for BFMO, while the E_R value quickly decreases from ~0.54 to ~0.19 eV for BFO. The E_R values are ~0.19 eV and ~0.36 eV for BFO and BFMO, indicating that hopping electrons and first ionization of oxygen vacancies are also responsible for the dielectric relaxation of the BFO and BFMO thin films, respectively, which is in accordance with the electrical conduction behavior. As mentioned above, the E is correlated to the density of oxygen vacancies.[46] Therefore, the BFMO thin film exhibits a lower density of oxygen vacancies than that of pure BFO under a low resistance state. The concentration of oxygen vacancies determines the leakage current density of BFO.[20−24] This present result well matches the lower leakage current density of BFMO observed in a high electric region, as shown in Figure 6. The similarity in the E_a value under different resistance states also confirms the electrical conduction mechanism is electric field-independent for BFMO, which is also in agreement with its leakage behavior.

4. CONCLUSION

The 5% Mn-modified $BiFeO_3$ thin film was deposited in situ on the $SrRuO_3/Pt/SiO_2/Si(100)$ substrate by rf sputtering. The migration kinetics of oxygen vacancies in the BFMO thin film was investigated in term of the temperature-independent impedance spectroscopy under different resistance states. The leakage current of the BFMO thin film is dominated by an Ohmic conduction regardless of varying temperatures and electric fields. The dielectric relaxation and electrical conduction of BFMO is governed by the thermal excitation of carriers from the first ionization of oxygen vacancies over the entire temperature range of 294 to 474 K, and is almost independent of the external electric fields, which is obviously different from those of BFO. The impedance spectroscopy in low and high resistance states successfully illuminates why the leakage current behavior of BFMO obviously differs from that of BFO in low and high electric field regions.

AUTHOR INFORMATION

Corresponding Author

*E-mail: wujiagang0208@163.com or msewujg@scu.edu.cn.

ACKNOWLEDGMENT

J.W. gratefully acknowledges the supports of the introduction of talent start funds of Sichuan University (2082204144033), the Sichuan University, and the National University of Singapore. The authors thank reviewers and the editor for their good comments and advice, which improve our paper.

REFERENCES

(1) Wu, J. G.; Wang, J. *Acta. Mater.* **2010**, *58*, 1688–1697.
(2) Li, J. F.; Wang, J. L.; Wuttig, M.; Ramesh, R.; Wang, N.; Ruette, B.; Pyatakov, A. P.; Zvezdin, A. K.; Viehland, D. *Appl. Phys. Lett.* **2004**, *84*, 5261–5263.
(3) Neaton, J. B.; Ederer, C.; Waghmare, U. V.; Spaldin, N. A.; Rabe, K. M. *Phys. Rev. B* **2005**, *71*, 014113.
(4) Teague, J. R.; Gerson, R.; James, W. J. *Solid State Commun.* **1970**, *8*, 1073–1074.
(5) Ramesh, R.; Spaldin, N. A. *Nat. Mater.* **2007**, *6*, 21–29.
(6) Eerenstein, W.; Mathur, N. D.; Scott, J. F. *Nature* **2006**, *442*, 759–765.
(7) Catalan, G.; Scott, J. F. *Adv. Mater.* **2009**, *21*, 2463–2466.
(8) Martin, L. W.; Chu, Y. H.; Ramesh, R. *Mater. Sci Eng., R* **2010**, *68*, 89–133.
(9) Dho, J.; Qi, X.; Kim, H.; MacManus-Driscoll, J. L.; Blamire, M. G. *Adv. Mater.* **2006**, *18*, 1445–1448.
(10) Wang, J.; Neaton, J. B.; Zheng, H.; Nagarajan, V.; Ogale, S. B.; Liu, B.; Viehland, D.; Vaithyanathan, V.; Schlom, D. G.; Waghmare, U. V.; Spaldin, N. A.; Rabe, K. M.; Wuttig, M.; Ramesh, R. *Science* **2003**, *299*, 1719–1722.
(11) Wu, J. G.; Kang, G. Q.; Wang, J. *Appl. Phys. Lett.* **2009**, *95*, 192901.
(12) Singh, S. K.; Ishiwara, H.; Sato, K.; Maruyama, K. *J. Appl. Phys.* **2007**, *102*, 094109.
(13) Wu, J. G.; Wang, J. *J. Appl. Phys.* **2009**, *106*, 054115.
(14) Murari, N. M.; Thomas, R.; Melgarejo, R. E.; Pavunny, S. P.; Katiyar, R. S. *J. Appl. Phys.* **2009**, *106*, 014103.
(15) Lee, C. C.; Wu, J. M. *Appl. Phys. Lett.* **2007**, *91*, 102906.
(16) Takahashi, K.; Tonouchi, M. *Jpn J. Appl. Phys.* Part 2. **2006**, *45*, L755-L758.
(17) Singh, S. K.; Ishiwara, H.; Maruyama, K. *Appl. Phys. Lett.* **2006**, *88*, 262908.
(18) Singh, S. K.; Menou, N.; Funakubo, H.; Maruyama, K.; Ishiwara, H. *Appl. Phys. Lett.* **2007**, *90*, 242914.
(19) Fujitsu Microelectronics America, Inc.: Sunnyvale, CA, 2 August 2006 (http://www.fujitsu.com/ca/en/news/pr/fma_20060802.html).
(20) Wu, J. G.; Wang, J. *J. Appl. Phys.* **2009**, *106*, 104111.
(21) Xiao, X.; Zhu, J.; Li, Y.; Luo, W.; Xu, B.; Fan, L.; Ren, F.; Liu, C.; Jiang, C. *J. Phys. D: Appl. Phys.* **2007**, *40*, 5775–5777.
(22) Li, Y.; Hu, Z.; Yue, F.; Yang, P.; Qian, Y.; Cheng, W.; Ma, X.; Chu, J. *J. Phys. D: Appl. Phys.* **2008**, *41*, 215403.
(23) Qi, X.; Dho, J.; Tomov, R.; Blamire, M. G.; MacManus-Driscoll, J. L. *Appl. Phys. Lett.* **2005**, *86*, 062903.
(24) Wang, C.; Takahashi, M.; Fujino, H.; Zhao, X.; Kume, E.; Horiuchi, T.; Sakai, S. *J. Appl. Phys.* **2006**, *99*, 054104.
(25) Mihara, T.; Watanabe, H.; de Araujo, C. A. P. *Jpn. J. Appl. Phys., Part 1* **1994**, *33*, 5281–5286.
(26) Damjanovic, D. *Rep. Prog. Phys.* **1998**, *61*, 1267–1324.
(27) Brazier, M.; Mansour, S.; McElfresh, M. *Appl. Phys. Lett.* **1999**, *74*, 4032–4034.
(28) Dawber, M.; Scott, J. F. *Appl. Phys. Lett.* **2000**, *76*, 1060–1062.
(29) Scott, J. F.; Dawber, M. *Appl. Phys. Lett.* **2000**, *76*, 3801–3803.
(30) Tagantsev, A. K.; Stolichnov, I.; Colla, E. L.; Setter, N. *J. Appl. Phys.* **2001**, *90*, 1387–1402.
(31) Zhong, Z.; Ishiwara, H. *Appl. Phys. Lett.* **2009**, *95*, 112902.
(32) Lee, K. W.; Kim, Y. I.; Lee, W. J. *Ferroelectrics* **2002**, *271*, 179–185.
(33) Jung, S. W.; Lee, J. G.; Kim, J. Y. *J. Korean Phys. Soc.* **1998**, *32*, S1710–S1713.
(34) Lee, J. J.; Thio, C. L.; Desu, S. B. *Phys. Status. Solidi. A* **1995**, *151*, 171–182.
(35) Schottky, W. *Naturwiss.* **1938**, *26*, 843–848.
(36) Mott, N. F.; Gurney, R. W. *Electronic Processes in Ionic Crystals*; Clarendon: Oxford, 1940.
(37) Frenkel *J. Tech. Phys. USSR* **1938**, *5*, 685.
(38) Sze, S. M. *Physics of Semiconductor Devices*, 2nd ed.; Wiley: New York,1981; Vol. 1, p 28.
(39) Iakovlev, S.; Solterbeck, C.-H.; Kuhnke, M.; Es-Souni, M. *J. Appl. Phys.* **2005**, *97*, 094901.
(40) Yang, H.; Jain, M.; Suvorova, N. A.; Zhou, H.; Luo, H. M.; Feldmann, D. M.; Dowden, P. C.; DePaula, R. F.; Foltyn, S. R.; Jia, Q. X. *Appl. Phys. Lett.* **2007**, *91*, 072911.
(41) Pabst, G. W.; Martin, L. W.; Chu, Y. H.; Ramesh, R. *Appl. Phys. Lett.* **2007**, *90*, 072902.

(42) Jonscher, A. K. *Dielectric Relaxation in Solids*; Chelsea Dielectrics: London, 1983.
(43) Bowen, C. R.; Almond, D. P. *Mater. Sci. Technol.* **2006**, *22*, 719–724.
(44) Srivastava, A.; Garg, A.; Morrison, F. D. *J. Appl. Phys.* **2009**, *105*, 054103.
(45) Viehland, D.; Jang, S. J.; Cross, L. E.; Wuttig, M. *J. Appl. Phys.* **1990**, *68*, 2916–2921.
(46) Steinsvik, S.; Bugge, R.; Gjonnes, J.; Tafto, J.; Norby, T. *J. Phys. Chem. Solids* **1997**, *58*, 969–976.